

# Three dimensional ferromagnetic architectures with multiple metastable states

F. Nasirpour<sup>1,\*</sup>, M. Engbarth<sup>2</sup>, S. J. Bending<sup>2</sup>, L. M. Peter<sup>3</sup>, A. Knittel<sup>4</sup>, H. Fangohr<sup>4</sup>, and M. V. Milošević<sup>5</sup>

<sup>1</sup>Department of Materials Engineering, Sahand University of Technology, Tabriz 51335-1996, Iran

<sup>2</sup>Department of Physics, University of Bath, Bath BA2 7AY, UK

<sup>3</sup>Department of Chemistry, University of Bath, Bath BA2 7AY, UK

<sup>4</sup>School of Engineering Sciences, University of Southampton, SO17 1BJ, Southampton, United Kingdom

<sup>5</sup>Departement Fysica, Universiteit Antwerpen, Groenenborgerlaan 171, B-2020 Antwerpen, Belgium

We demonstrate controllable dual-bath electrodeposition of nickel on architecture-tunable three dimensional (3D) silver microcrystals. Magnetic hysteresis loops of individual highly faceted (HF) Ag-Ni core-shell elements reveal magnetization reversal that comprises *multiple sharp steps* corresponding to different stable magnetic states. Finite-element micromagnetic simulations on smaller systems show several jumps during magnetization reversal which correspond to transitions between different magnetic vortex states. Structures of this type could be realizations of an advanced magnetic data storage architecture whereby each element represents one multi-bit, storing a combination of several conventional bits depending on the overall number of possible magnetic states associated with the 3D core-shell shape.

PACS numbers: 81.15.Pq, 75.70.-i, 75.60.Ej, 75.78.Cd

Recent advances in nanofabrication and synthetic chemistry have lead to a dramatic growth in research activity in the area of magnetic nanostructures [1], with key applications in data storage, medical diagnosis and quantum information processing. Much of the work has focused either on lithographically patterned thin films or nanoscale particles and clusters. In contrast, very little work has been attempted on 3D mesostructures, whose sizes are comparable with the relevant characteristic physical lengthscales (e.g., ferromagnetic domain size and domain wall width). It has been recently [2] demonstrated that “architecture-tunable” mesostructures can be grown by electrodeposition onto highly oriented pyrolytic graphite (HOPG) substrates. These structures are perfectly 3D in stark contrast to lithographically patterned structures, which invariably have rough edges and surfaces.

The main objective of this Letter is to point out the correlation between HF structures and their magnetic properties. For example, it is already known that the shape of magnetic micro- or nanostructures has pronounced effects on magnetic anisotropy [3]. We use electrodeposition, a procedure by which Pb, Ag, Bi and Sn can be readily deposited in the form of HF microcrystals [4-6], while nickel is found to form wires or particles without any recognizable facets. In what follows, we report the fabrication and magnetic characterization of HF, 3D Ni mesostructures, using a dual-bath method [7]. We argue that the 3D shape of the sample hosts many more stable magnetic states than 2D analogues, and hence can be used for multi-bit data storage.

Electrodeposition was carried out under potentiostatic mode in a conventional three-electrode cell connected to a potentiostat (microAutolab III) using HOPG as working electrode, a platinum plate as counter electrode and a standard Ag/AgCl electrode and high-purity silver wire as reference electrodes. To establish appropriate deposition potentials,

cyclic voltammograms (CV) were captured in the prepared electrolytes.

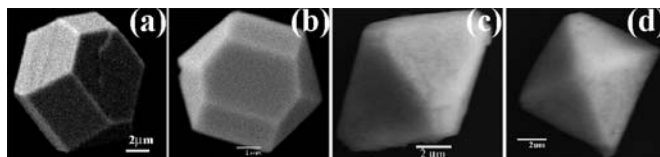


FIG. 1: Different shapes of silver mesocrystals electrodeposited at (a) - 60 mV for 10 sec from 250 mM Ag nitrate (b) -60 mV for 30 sec from 100 mM Ag nitrate, (c) -70 mV for 20 sec from 100 mM Ag nitrate and (d) 1 V for 60 sec followed by 10 seconds at open circuit potential and finally -10 mV for 30 sec from 100mM Ag nitrate.

A two-step dual-bath potentiostatic method was used to electrodeposit Ag-Ni core-shell structures. In the first step, HF silver mesocrystals were electrodeposited from nitrate electrolytes at a pH=2-2.5. The sample was then gently rinsed in deionized water and blow dried with argon. In the second step nickel was electrodeposited from a Watts bath containing 2.3 mol/L H<sub>2</sub>O Ni sulphate, 0.6 mol/L H<sub>2</sub>O Ni chloride, and 0.5 mol/L H<sub>2</sub>O boric acid, with a pH=3-4. The thickness of the nickel shell was determined from Faraday's law with a cathodic current efficiency of 100% using the computer-controlled deposition software (Autolab-GPES). For the given surface area of the working electrode and the effective surface density of silver islands, the nickel thickness was estimated to be 100 nm from the known total charge passing through the cell (the For instance, for the pyramid structure shown in Fig. 1d, a total charge of 16 mC was conducted to obtain a 100 nm thick Ni film.

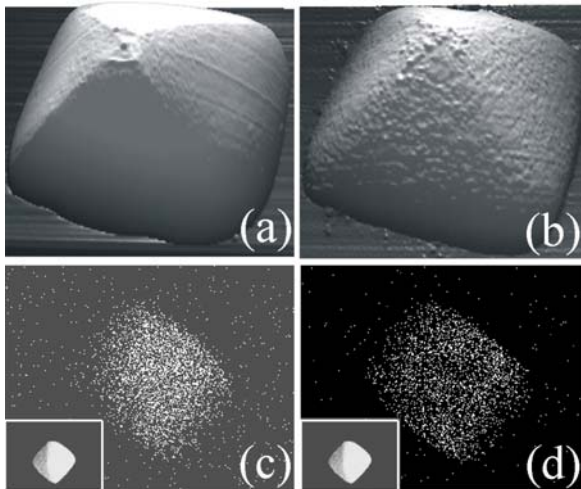


FIG. 2: (a) 3D AFM image of a typical Ag pyramidal mesocrystal with the height from the base to the apex of  $5.2 \mu\text{m}$  and  $10 \mu\text{m}$  base sidelength, (b) Ag mesocrystal after electrodeposition of a 100 nm Ni shell on top. EDS elemental maps of silver (c) and nickel (d) taken on the actual Ag-Ni mesocrystal as shown in insets.

The scanning electron micrographs of the electrodeposited HF silver mesocrystals with different sizes and shapes are shown in Figure 1. A Ni shell was subsequently electrodeposited on silver mesocrystals from a Watts bath at a potential of  $-800 \text{ mV}_{\text{Ag}/\text{AgCl}}$ . CVs taken in the Watts bath on bare HOPG and with silver electrodeposited on HOPG, showed a considerable difference in the equilibrium deposition potential of nickel. When nickel is electrodeposited on the bare HOPG, it starts to reduce at potentials more negative than  $-840 \text{ mV}_{\text{Ag}/\text{AgCl}}$ . In the presence of silver metallic centers on HOPG, nickel starts to grow at potentials more negative than  $-670 \text{ mV}_{\text{Ag}/\text{AgCl}}$ . At this potential, the nickel shell is solely electrodeposited on the silver centers. Ex-situ atomic force micrographs (AFM) taken from a pyramidal silver mesocrystal before and after electrodeposition of nickel are shown in Figs. 2 (a) and (b). Surface roughening of the polycrystalline nickel shell is clearly seen as a result of the well-established 3D nucleation and growth mechanism of electrodeposition of nickel [8] or due to the presence of hydrogen evolution [9] on the crystalline Ag core. The energy dispersive X-ray spectroscopy (EDS) elemental maps show that nickel is primarily deposited on top of the silver mesocrystals, as seen in Figs. 2 (c) and (d). Both maps exhibit modest signal to noise levels because of the inherent noise background in EDS. However, the accumulation of a high density of pixels in the vicinity of the core-shell is good evidence of highly local electrodeposition.

We carried out the magnetic  $M_z$ - $H_z$  measurements at 5K on individual Ag-Ni core-shell structures directly placed with the apex pointing upwards on a linear array of  $2 \mu\text{m} \times 2 \mu\text{m}$  GaAs/AlGaAs heterostructure Hall probes, where  $z$  is the direction perpendicular to the plane of the Hall probe. An external magnetic field was applied perpendicular to the Hall

array. Figure 3 shows the magnetization curves obtained for one particular pyramid [Fig. 1(d)] and a truncated icosahedron [Fig. 1(b)] at the same applied field sweep rate. Surprisingly, the magnetization reversal occurs in a *stepwise fashion* in both hysteresis loops. Each step corresponds to a different, stable magnetic state, as verified by performing minor loops (back-tracking) for several magnetization steps. Minor loops were recorded by sweeping the magnetic field to different levels after saturating the sample in the opposite direction. Depending on the magnetic history, we find *six* different stable states at zero magnetic field for the pyramidal structure, and *ten* for the more complex icosahedral shaped magnetic element. In Fig. 3b, the magnetic states decay relatively fast upon reversal of the magnetic field. This is a consequence of a rather thick Ni shell of the sample. Namely, the metastability of magnetic states in 3D ferromagnets is mainly due to different demagnetization scenarios in the vicinity of 3D edges. As thinner shells will have the more pronounced (sharp) edges, more possible states and their enhanced stability can be expected.

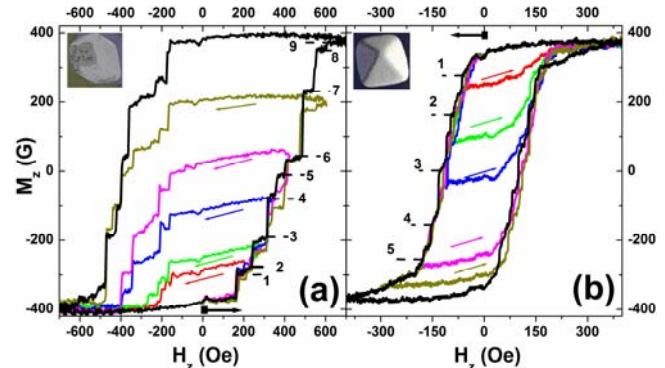


FIG. 3: Hysteresis loops and back-tracking curves of a (a) truncated icosahedral and (b) pyramidal Ag-Ni structure with a typical 100 nm nickel shell (shown in upper left insets) measured in an external magnetic field applied perpendicular to the base of the element at 5K. Arrows show the directions of application of magnetic field and backward sweep to obtain minor loops. Dashed lines indicate the positions of magnetization steps. Note: the full hysteresis loop is shifted horizontally to the left by a magnitude of 20 Oe for clarity.

Figure 3 demonstrates not only existence of different magnetic states for our 3D mesostructures, but also the controllable, sharp switching between different magnetization states. These two properties are essential for a data storage element like conventional magnetic binary bits or quaternary (4-state) bits based on the vortex chirality or its polarization [10]. However, although an electronic method for reversing vortex polarity has already been established [11], reversing the chirality in a reproducible way is still a formidable task. The 3D architecture of our magnetic elements offers a simple alternative either for multi-bit storage, or storage of a combination of conventional bits ( $2^n$  magnetic states needed to store all combinations of  $n$  bits). The scalability of our mesostructures for this application is possible by making them far smaller as they become faceted practically

immediately upon electrochemical nucleation. The only reason that we report data here on micron-sized crystals is because the manipulation and Hall probe magnetometry is greatly facilitated in larger samples.

To verify the above scenario we have used the finite-element, micromagnetic solver Nmag [12] with hierarchical matrices [13] in order to simulate the magnetization process of pyramidal shell structures. The magnetocrystalline anisotropy of nickel is neglected in our model and is reasonable at room temperature when the cubic anisotropy of Nickel is small. Stronger deviations may be expected between simulation and experiment as we performed experiments at low temperatures only to reduce the noise of the Hall sensor. Figure 4 shows the obtained simulation results for the reversal behavior of a Ni pyramidal shell of Fig. 2 but scaled down by a factor of 20. This down-scaling is necessary in order to perform computationally feasible simulations, but is also more suited for the data storage concept. We indeed find that the spatially averaged magnetization undergoes several jumps during the reversal process, via different 3D magnetic vortex states. Our simulations are still very computationally challenging, as the mesh resolution has to be significantly smaller than the shell thickness. Mirroring our experiments, we have backtracked the observed magnetic states revealing the stability of four vortex states at  $H_{\text{ext}}=0$  Oe, with (i) the core of the vortex on the top of the pyramidal structure (symmetric state, inset (a) in Fig. 4), or (ii) the core on one of the side faces (asymmetric vortex state, insets (b) and (c) in Fig. 4). The states of figure 4b and 4c do not only differ in the vortex core position but also in the way the magnetization curls around the core. A closer comparison between these states reveals that, on average, the z-component of the state in figure 4c is more negative. High demagnetization fields that occur in the vicinity of the sharp edges, which separate the triangular faces, lead to the energetic differences between the observed vortex states. Our simulations are done at  $T=0\text{K}$ , but the calculated energy differences between the micromagnetic states are in the eV range and thus can be thermally stable at higher temperatures (for energy barrier  $E_M$  as the mean value of the activation energy  $E$ , to other states exceeding  $50K_B T$  [14,15]).

This work was supported by EPSRC in the UK under grants EP/E039944/1 and EP/E040063/1, DYNAMAG project (EU FP7/2007-2013 Grant No. 233552), and FWO-Vlaanderen.

\*Electronic address: nasirpour@sut.ac.ir

- [1] F. Nasirpour, A. Nogaret in *Nanomagnetism and Spintronics* (World Scientific, Singapore, 2010).
- [2] Z. L. Xiao, C. Y. Han, W.-K. Kwok, H. Wang, U. Welp, J. Wang, G. W. Crabtree, *J. Am. Chem. Soc.* 126, 2316 (2004).
- [3] C. A. Ross, *Annu. Rev. Mater. Res.* 31, 203 (2001).
- [4] M. P. Zach, K. H. Ng, and R. M. Penner, *Science* 290, 2120 (2000).

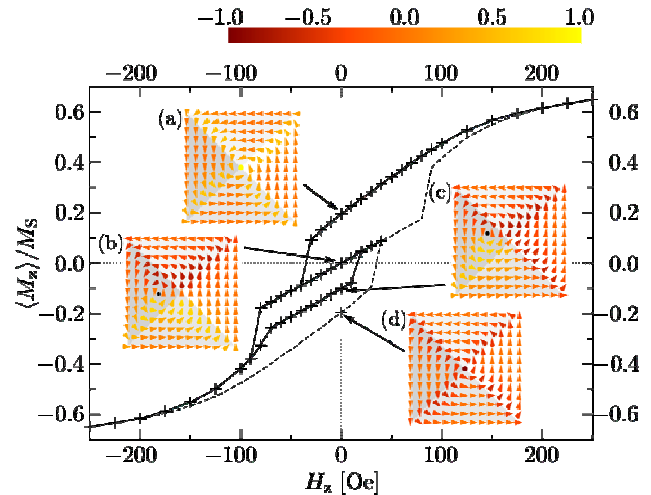


FIG 4: The magnetization loops and micromagnetic states from a top-down perspective with z-component magnetization color bar obtained by micromagnetic simulations, for a pyramidal Nickel shell with a base side length of 500 nm, a height of 250 nm, and thickness of 5nm. The calculated, spatially averaged magnetization  $\bar{M}$  is normalized with respect to the saturation magnetization ( $M_S=510000\text{A/m}$ ). The dashed line is the mirror image of the reversal curve. Inset (a) shows a symmetric vortex with its core sitting on the top of the shell. Insets (b) and (c) show the asymmetric vortex state, where the core (indicated by black dots) sits on one of the side faces. Point (d) corresponds to the reversed symmetric vortex state (not shown due to a lack of space). The states have the following micromagnetic energies: (a) and (d) 26.6 eV, (b) 22.0 eV and (c) 24.0 eV.

- [5] A. E. Muller, S. E. C. Dale, M. A. Engbarth, S. J. Bending, and L. M. Peter, *Cryst. Eng. Comm.* 12, 2135 (2009).
- [6] S. E. C. Dale, S. J. Bending, and L. M. Peter, *Langmuir*, 25 11228 (2009).
- [7] A. Blondel, B. Doudin, and J.-Ph. Ansermet, *J. Magn. Magn. Mater.* 165, 34 (1997).
- [8] S. Morin, A. Lachenwitzer, O. M. Magnussen, and R. J. Behm, *Phys. Rev. Lett.* 83, 5066 (1999).
- [9] W. Schwarzacher, *J. Phys.: Condens. Matter* 16, R859 (2004).
- [10] C. Phatak, M. Tanase, A. K. Petford-Long, and M. De Graef, *Ultramicroscopy* 109, 264 (2009).
- [11] K. Yamada, S. Kasai, Y. Nakatani, K. Kobayashi, H. Kohno, A. Thiaville, and T. Ono, *Nature Materials* 6, 270 (2007).
- [12] T. Fischbacher, M. Franchin, G. Bordignon, and H. Fangohr, *IEEE Trans. Magn.* 43, 2896 (2007).
- [13] A. Knittel, M. Franchin, G. Bordignon, T. Fischbacher, S. J. Bending, and H. Fangohr, *J. Appl. Phys.* 105, 07D542 (2009).
- [14] H.N. Bertram and M. Williams, *IEEE Transactions on Magnetism*, 36, 1 (2000)
- [15] R.P. Cowburn, *J. Appl. Phys.*, 93, 9310 (2003)